



Contents lists available at ScienceDirect

Chemical Engineering Journal

journal homepage: www.elsevier.com/locate/cej

Significantly enhanced lithium storage by in situ grown $\text{CoS}_2@MoS_2$ core-shell nanorods anchored on carbon cloth

Shenyu Du^a, Cong Wu^a, Liyuan Ao^a, Xin Zhou^a, Kai Jiang^a, Liyan Shang^a, Yawei Li^a, Jinzhong Zhang^a, Zhigao Hu^{a,b,c,*}, Junhao Chu^{a,b,c}

^a Technical Center for Multifunctional Magneto-Optical Spectroscopy (Shanghai), Department of Materials, School of Physics and Electronic Science, East China Normal University, Shanghai 200241, China

^b Collaborative Innovation Center of Extreme Optics, Shanxi University, Taiyuan, Shanxi 030006, China

^c Shanghai Institute of Intelligent Electronics & Systems, Fudan University, Shanghai 200433, China

ARTICLE INFO

Keywords:

MoS_2
 CoS_2
 Core-shell
 Carbon cloth
 Lithium-ion battery

ABSTRACT

MoS_2 becomes one of the ideal anode materials for lithium-ion batteries (LIBs) because of its unique two-dimensional layered structure and high theoretical capacity. However, the poor conductivity and volume change during reaction hinder its application. In this work, we demonstrate a two-step hydrothermal method to synthesis the unique structure of core-shell $\text{CoS}_2@MoS_2$ nanorods anchored on carbon cloth (CC). The one-dimensional Co(OH)_2 nanowire array on CC forms a carbon-based framework, which increases the reaction surface area for subsequent in situ generation of MoS_2 . The MoS_2 layer with rich holes enhances lithium storage capacity and increases the active sites. Compared with pure MoS_2 electrode, $\text{CoS}_2@MoS_2/CC$ (CMCC) exhibits a stronger electrochemical performance as a binder-free electrode for LIBs. The structure has a high discharge specific capacity of 1175 mA h g^{-1} at the current density of 0.1 A g^{-1} . The further experiments prove that the CMCC structure has outstanding ion transport ability and low impedance characteristics, which are attributed to its special structure and the introduction of Co ions. The present work provides a new idea for the design of stable flexible electrode with high electrochemical performance for lithium-ion batteries.

1. Introduction

Due to the advantages of high energy density, high safety and long cycle life, lithium-ion battery has become one of the most potential energy storage devices in recent years [1–4]. In order to obtain better performance, quite a few studies have been carried out around the anode materials, and the use of transition metal sulfides (TMSs) is one of the effective strategies. Compared with traditional graphite anodes with a theoretical capacity of only 372 mAh g^{-1} , TMSs have attracted much attention due to their unique lithium storage mechanism, higher theoretical capacity and larger interlayer spacing [5–7]. For the above reasons, many researches on TMSs have been conducted [8–11]. Among them, MoS_2 has gradually become a potential candidate for electrode materials due to its high theoretical capacity (669 mAh g^{-1}), excellent stability and specific interlayer structure [12,13]. Particularly, MoS_2 has a two-dimensional layered structure, and the interlayer spacing of 0.62 nm facilitates the insertion of lithium ions among the layers and thus has a good lithium storage capacity. The adjacent S–Mo–S structure supplied active sites for electrochemical lithium storage. Then,

Li_2S and Mo are formed by insertion and redox reactions to provide a high theoretical capacity [14,15]. Although it has many advantages, the research progress and application are greatly restricted due to some important factors, such as low conductivity, large volume change, and poor long-term cycling stability during lithium ion storage [16–18].

Up to now, various optimization methods have been used to overcome these shortcomings. For example, MoS_2 can be combined with graphene [19], carbon nanotubes [20] and other carbon based materials [21–26]. Reasonably designed composite materials can often inherit many advantages of carbon-based materials, such as high conductivity, large area and structural ductility, thereby significantly improving the electron transport characteristics and structural stability of the electrode [27,28]. In this way, not only the conductivity can be enhanced, but also the MoS_2 stacking can be prevented effectively. Besides, the combination of MoS_2 and carbon materials may further improve the electrochemical properties of the composites. The structure design of MoS_2 can also solve the agglomeration problem and improve the stability of the electrode [29,30]. For example, Wang et al. compounded

* Corresponding author at: Technical Center for Multifunctional Magneto-Optical Spectroscopy (Shanghai), Department of Materials, School of Physics and Electronic Science, East China Normal University, Shanghai 200241, China.

E-mail address: zghu@ee.ecnu.edu.cn (Z.G. Hu).

<https://doi.org/10.1016/j.cej.2020.127714>

Received 24 August 2020; Received in revised form 19 October 2020; Accepted 9 November 2020

Available online 13 November 2020

1385-8947/© 2020 Elsevier B.V. All rights reserved.

MoS₂ with carbon to form a porous structure, and achieved a specific capacity of 707 mAh g⁻¹ at a density of 0.2 A g⁻¹ and maintained good stability after 500 cycles [31]. Zhou et al. used a two-dimensional space confinement strategy to fix a few layers of molybdenum sulfide to the surface of carbon nanosheets, and still maintain a high specific capacity of 430 mAh g⁻¹ at a current density of 10 A g⁻¹ [32]. Moreover, our previous work reported that a novel carbon-sealed vertical MoS₂-SnO₂ (C@MoS₂-SnO₂@Gr) material polymerized in situ on graphene aerogel was used as a lithium-ion battery negative electrode. The three-dimensional structure formed by the carbon layer and the graphene matrix provides a continuous conductive network for electron/ion diffusion. The synergistic effect between MoS₂ nanosheets and SnO₂ particles can enhance the charge transfer kinetics. The C@MoS₂-SnO₂@Gr can provide a stable capacity of 680 mA h g⁻¹ for 2000 cycles at 2.5 A g⁻¹ [33]. However, due to the limitation of its inherent ion transport mechanics, the properties of electrode materials are often deteriorated. Therefore, doping is often used as an effective strategy. Wang et al. reported the modification of MoS₂ electrode by Mn ion doping [34]. The intercalation of Mn ions extends the layer spacing of MoS₂, facilitates the transport of lithium ion and improves the conductivity of the electrode. Moreover, Li et al. found that the introduction of Co into MoS₂ can significantly improve the electrochemical properties of the materials [35]. The synergistic effect of this structure can effectively inhibit the stacking of MoS₂ in the cycle process and enhance the stability of the reaction, thus greatly extending the battery life.

Here, we demonstrate a simple synthesis of flexible lithium-ion battery anode electrode, in which CoS₂ nanorods coated with MoS₂ layer are anchored on carbon cloth (denoted as CMCC) by stepwise hydrothermal method. During the synthesis process, the one-dimensional dense cobalt hydroxide nanoneedles on the surface of the carbon cloth increase the contact area of the reaction. It is subsequently vulcanized into a CoS₂ core so that the MoS₂ covering layer grew in situ and anchored to the carbon fiber. Compared with other reference experiments, this structure shows better stability and specific capacity in cycle and rate tests. In addition, the core-shell structure can effectively alleviate the volume change and agglomeration problems of MoS₂ during the electrochemical reaction. Also, the porous surface morphology provides more lithium storage points. The electrochemical impedance analysis spectrum further proves that the existence of Co ions reduces the charge transfer resistance of the electrode. Therefore, CMCC electrodes exhibit excellent electrochemical characteristics for lithium ion batteries.

2. Experimental section

2.1. Synthesis of Co(OH)₂/CC

Carbon cloth (CC) was ultrasonically cleaned with acetone, deionized water and ethanol for 20 min, respectively. After dried in vacuum oven, O₂-plasma (air, 50 W, 0.3 torr) was provided and lasted for 15 min. Generally, 1.36 mm CoCl₂ · 6H₂O, 18.0 mm NH₄Cl and 5.99 mm CO(NH₂)₂ were added to 20 mL deionized (DI) water with continuously stirring for 30 min and then transferred into a Teflon-lined stainless autoclave (50 mL). A piece of plasma-treated CC (3 cm × 2 cm) was immersed into the above solution and heated at 120 °C for 6 h. After cooling down to room temperature, the CC with pink product was washed with DI water for several times and dried at 70 °C overnight.

2.2. Synthesis of CoS₂@MoS₂/CC

Briefly, 0.12 mm Na₂MoO₄ · 2H₂O and 0.79 mm thiourea were successively dissolved in 20 mL of deionized water. Then the solution was kept in a Teflon-lined stainless autoclave (50 mL) and the as-synthesized Co(OH)₂/CC sample was immersed into it. Finally, the autoclave was sealed and heated to 200 °C for 24 h. The product was gathered by rinsing with deionized water and ethanol, then dried in

vacuum at 70 °C for 10 h. The average mass of CoS₂@MoS₂ loaded on the CC was about 2.4 mg cm⁻². Correspondingly, the weight of CoS₂ and MoS₂ on the CC were about 2.02 and 1.83 mg cm⁻², respectively. In contrast, CoS₂/CC could be gained with the similar method without adding Na₂MoO₄. The MoS₂/CC was also produced by using plasma-treated CC instead of Co(OH)₂/CC. CoS₂@MoS₂ can be obtained by reaction without adding CC. Specifically, Co(OH)₂ nanoneedles can be obtained without adding CC in the first step, which is washed with deionized water and dried at 70 °C overnight. Then, 30 mg Co(OH)₂, 30 mg Na₂MoO₄ and 60 mg thiourea were added to 20 mL of deionized water in sequence, followed by a hydrothermal reaction at 200 °C for 24 h to obtain CoS₂@MoS₂.

2.3. Material characterization

In the scanning range of 10° to 80°, the crystal structure of the final product was tested by X-ray diffraction (XRD, Bruker D8 Advance diffractometer) with Cu-K_α radiation (λ = 1.5418 Å). A Jobin-Yvon LabRAM HR 800 micro-Raman equipped with a 532 nm laser was operated for Raman spectroscopy measurements. A RBD upgraded PHI-5000C ESCA system with Mg-K_α radiation (hν = 1253.6 eV) was operated to study the X-ray photoelectron spectroscopy (XPS). To further analyze the morphology and structure of the sample, the scanning electron microscopy (SEM) images and the transmission electron microscopy (TEM) images were collected by a PHILIPS XL30TMP system and an FEI Tecnai G2 F20 TEM with an experimental voltage of 200 KV, respectively.

2.4. Electrochemical measurements

The electrochemical performances of CoS₂@MoS₂/CC NRs were investigated in CR2025 coin type half-cell, which was fabricated in a glove box filled with argon gas. CoS₂@MoS₂/CC was directly used as electrode without binder and lithium foil worked as counter electrode. CoS₂@MoS₂ electrode was prepared by slurry preparation. The active material, acetylene black and polyvinylidene fluoride binder (PVDF) were added to N-methyl-2-pyrrolidone (NMP) solvent in a ratio of 7:2:1 and stirred thoroughly to obtain a slurry. Then it was evenly coated on the copper foil and dried at 80 °C in vacuum overnight. The loading mass of the electrode was about 0.8–1.0 mg cm⁻². 1 M LiPF₆ was dissolved in ethylene carbonate, dimethyl carbonate and ethyl methyl carbonate at a volume ratio of 1:1:1 as electrolyte, and Celgard 2400 membrane was employed as a separator. The LAND battery test station was used to perform the galvanostatic cycling tests with the voltage range of 0.01–3.0 V (vs. Li⁺/Li). Cyclic voltammetry (CV) curves at different scan rates were tested with the CHI660E electrochemical workstation and the frequency range of electrochemical impedance spectroscopy (EIS) is 100 kHz to 0.01 Hz.

3. Results and discussion

The synthesis process of the CoS₂@MoS₂/CC structure is shown in Fig. 1. Firstly, oxygen-containing functional groups such as hydroxyl group and carboxyl group were attached on the surface of carbon fiber by O₂ plasma treatment, which promoted the subsequent hydrothermal reaction [36]. Next, the O₂-treated carbon cloth was placed into the precursor solution to generate acicular Co(OH)₂ nanoarrays (NAs) on its surface (Fig. 3a). In the subsequent hydrothermal process, Co(OH)₂ NAs react with thiourea solution. Due to the Kirkendall effect and anion exchange [37], Co ions diffuse inward faster than sulfur ions outward, which makes Co(OH)₂ NAs react with S ions to form CoS₂ nanorods. At the same time, the surface of CoS₂ was coated with MoS₂ nanoflakes synthesized by thiourea and Na₂MoO₄. It can be seen that the formation of CoS₂ nanorods using Co(OH)₂ as template and coating the outer layer of MoS₂ can be achieved simultaneously, which ensures the high efficiency of synthesis. The advantages of CoS₂@MoS₂/CC

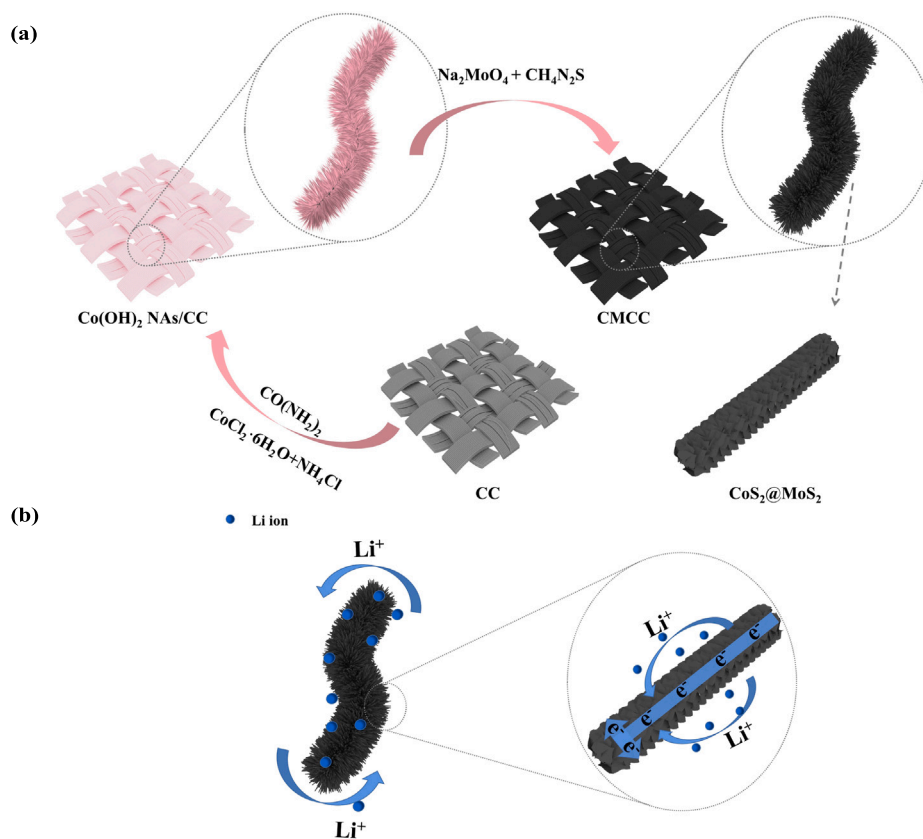


Fig. 1. (a) Schematic illustration for the synthetic route of the core-shell structure $\text{CoS}_2\text{@MoS}_2/\text{CC}$. (b) Schematic illustration of the transmission path of lithium ions and electrons in the $\text{CoS}_2\text{@MoS}_2/\text{CC}$ electrode.

as anode materials for lithium-ion batteries are shown in Fig. 1a. A thin layer of MoS_2 nanoflakes is coated on the surface of cobalt sulfide and anchored on the surface of carbon fiber, which improves the conductivity and capacity, and made the structure more stable. In addition, the core-shell structure can alleviate the volume change during the redox process and effectively prevent the agglomeration and accumulation of MoS_2 nanoflakes. As highlighted in Fig. 1b, the CMCC system structure has excellent electrochemical capabilities as a LIB anode. One-dimensional CoS_2 nanorods anchored on the surface of the carbon cloth provide attachment points for MoS_2 with a large interlayer spacing. This structure improves the conductivity and stability of the electrode, so it can efficiently and stably transport lithium ions and electrons. The core-shell structure provides sufficient space for volume expansion and effectively inhibits the agglomeration and accumulation of MoS_2 in the reaction.

The simulation of reaction kinetics can be used to briefly discuss the second step [38,39]. In order to realize the formation of CoS_2 nanorods and the coating of MoS_2 nanoflakes at the same time, the key is to match the reaction rate of the two progress. In the first order reaction, the reaction rate is related to the concentration, so we can express the relative rate between CoS_2 and MoS_2 by the ratio of reaction rate $R_{\text{CoS}_2/\text{MoS}_2}$ [40]. The following formula can be obtained:

$$R_{\text{CoS}_2/\text{MoS}_2} = \frac{c_{\text{CoS}_2}^{(l)}(r)/c_{\text{CoS}_2}^{(0)}}{c_{\text{MoS}_2}^{(l)}(r)/c_{\text{MoS}_2}^{(0)}} = k_{\text{CoS}_2/\text{MoS}_2} (1-d)^{\left(1 - \frac{1}{k_{\text{CoS}_2/\text{MoS}_2}}\right)} \quad (1)$$

where $k_{\text{CoS}_2/\text{MoS}_2} = k_{\text{CoS}_2}/k_{\text{MoS}_2}$

$c_{\text{CoS}_2}^{(l)}(r)$ and $c_{\text{MoS}_2}^{(l)}(r)$ in the formula are the local concentrations of CoS_2 and MoS_2 , respectively, and $c_{\text{CoS}_2}^{(0)}$ and $c_{\text{MoS}_2}^{(0)}$ represent the total concentrations of CoS_2 and MoS_2 , respectively. For $k_{\text{CoS}_2/\text{MoS}_2}$, we can get the following derivation by combining with Arrhenius equation:

$$k_{\text{CoS}_2/\text{MoS}_2} = e^{\frac{2(d_B^{(0)} - T_A^{(0)})}{T}} \quad (2)$$

The value of $T_B^{(0)} - T_A^{(0)}$ in the present work is 20 K, and the relationship between $k_{\text{CoS}_2/\text{MoS}_2}$ and temperature (T) is shown in Fig. 2a. It is not difficult to find that the value of $R_{\text{CoS}_2/\text{MoS}_2}$ is close to 1, which indicates that the reaction rate of CoS_2 is close to MoS_2 (Fig. 2b). It proves that the synthesis of CoS_2 nanorods is accompanied by the coverage of MoS_2 nanoflakes. With the reaction going on, the value of $R_{\text{CoS}_2/\text{MoS}_2}$ almost did not change. It indicates that 473 K is the optimal temperature for simultaneous reaction.

The scanning electron microscopy (SEM) characterization at different magnification were carried out to further study the morphology of the samples. As shown in Fig. 3a, urchin-like Co(OH)_2 NAs are densely grown on the CC with smooth surfaces and the diameter of 300–400 nm. Different from the bare carbon cloth (Fig. S1†), the designed cobalt hydroxide nanoarrays can increase the contact area and provide loading sites for subsequent reactions. Moreover, carbon fibers provide channels for ion transport and enhance the conductivity. Fig. 3d–f shows the SEM images of CMCC at different magnification. Obviously, the sample has a prominent one-dimensional nanotube morphology with a uniform diameter of about 400–500 nm, which basically retains the characteristics of the previous nanoarray (Fig. 3a). In addition, the independent CoS_2 and MoS_2 as shown in Fig. 3b and Fig. 3c are not observed in the field of view of large magnification, indicating that the product is formed by the close combination of MoS_2 and CoS_2 . Further magnification shows that the surface of each nanotube is covered with interconnected nanoflakes of MoS_2 (Fig. 3d–f), and a large amount of voids are formed to increase the contact area. This structure provides more active sites for lithium ion reaction and promotes the diffusion of ions and electrons in the process, which leads to excellent lithium storage performance. To further analyze the structure, CMCC was characterized by transmission electron microscopy (TEM). In Fig. 4a–c, the coverage of MoS_2 can be observed at different magnification, which corresponds to the SEM morphology. The comparison proves

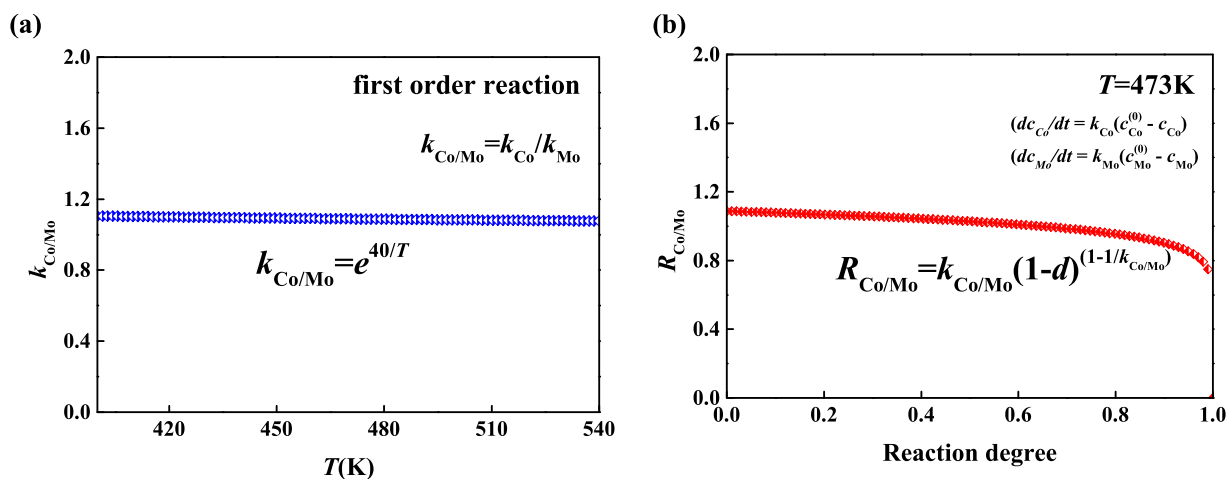


Fig. 2. (a) Dependence of $k_{\text{CoS}_2/\text{MoS}_2}$ on reaction temperature. (b) The relationship between $R_{\text{CoS}_2/\text{MoS}_2}$ and reaction degree.

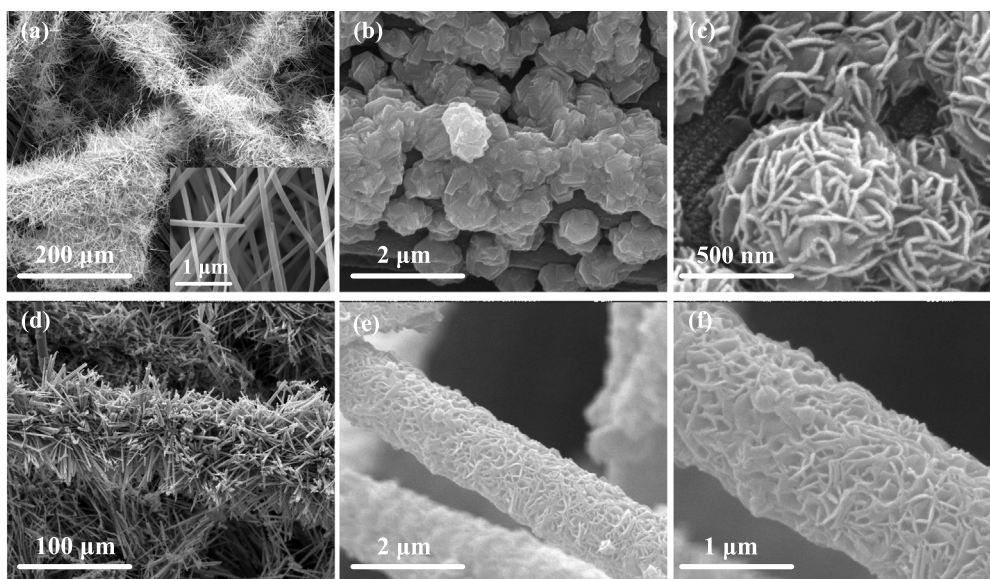


Fig. 3. (a)–(c) SEM images of Co(OH)₂/CC, CoS₂/CC and MoS₂/CC, respectively. (d)–(f) High-magnification SEM images of CoS₂@MoS₂/CC, respectively.

that CoS₂ and surface MoS₂ constitute a core–shell structure. It can be noted that the final product basically maintains the structure of the precursor and realizes the tight in situ growth of MoS₂. In addition, high-resolution TEM (HRTEM) shows that the interlayer spacing of the nanoflakes is 0.62 nm, which matches with the (002) phase of MoS₂ (Fig. 4d). The EDS element mapping images in e–h show the elemental composition and distribution. The Mo and S elements almost cover the entire sample, which indicates that MoS₂ forms a uniform coating on the surface. The distribution of Co, Mo and S highlights the close combination of the core–shell structure, which cannot only reduce the volume expansion during the redox reaction, but also alleviate the accumulation of MoS₂.

Fig. 5a shows the X-ray diffraction (XRD) pattern of the first hydrothermal product, which matches with Co(OH)₂ (JCPDS No. 38-0547). In Fig. 5b, the diffraction peaks of CMCC at $2\theta = 32.2^\circ$, 36.2° , 39.8° and 54.9° are consistent with (200), (210), (211) and (311) crystal faces of CoS₂ (JCPDS No. 41-7417), respectively. The results show that the nanorods have good crystallinity and no impurities such as Co₃O₄ and Co₉S₈ can be observed. The broad diffraction peaks between 20° and 30° are matched with the carbon cloth. It can be noted that no obvious MoS₂ diffraction peak can be observed, which may be caused by the low thickness of MoS₂ with few layers in the sample. On

the other hand, two distinct characteristic peaks are observed at 378.6 and 405.1 cm⁻¹ in the Raman spectrum, which belong to the E_{2g}¹ and A_{1g} modes of MoS₂, respectively (Fig. 5c) [41]. It confirms the synthesis of a uniform MoS₂ coating on the surface of the CMCC. In addition, the characteristic peaks at 1348.1 and 1594.5 cm⁻¹ represent the D and G vibration bands of the CC substrate, respectively [42].

The element distribution and valence states of the CMCC were further analyzed by XPS. According to Fig. 6a, the sample contains Co, Mo, S, O and C elements, where C is assigned to the carbon cloth substrate peak. Accordingly, the O element mainly attributed to the use of O₂-plasma in the pretreatment process. In the electron curve of Co 2p, the peaks of 779.5 and 795.4 eV correspond to Co 2p_{3/2} and Co 2p_{1/2}, respectively (Fig. 6b) [43]. Two distinct satellite peaks corresponding to Co–O bond are also observed at 785.1 and 801.4 eV, which may be due to the close binding of CoS₂ to CC under the action of oxygen-containing functional groups [44,45]. After fitting the curve of Mo 3d in Fig. 6c, two peaks of 230.6 and 233.8 eV can be obtained, which represent the Mo_{5/2} and Mo_{3/2}, respectively [46,47]. In addition, the orbital peak of S 2s can be seen at 223.3 eV. In Fig. 6d, the peaks at 162.9 and 163.8 eV of S 2p_{3/2} and S 2p_{1/2} belong to S²⁻ in the complex. The atomic contents of C, Co, Mo and S in CMCC are fitted to be 47.85, 8.62, 6.86 and 5.85 at%, respectively.

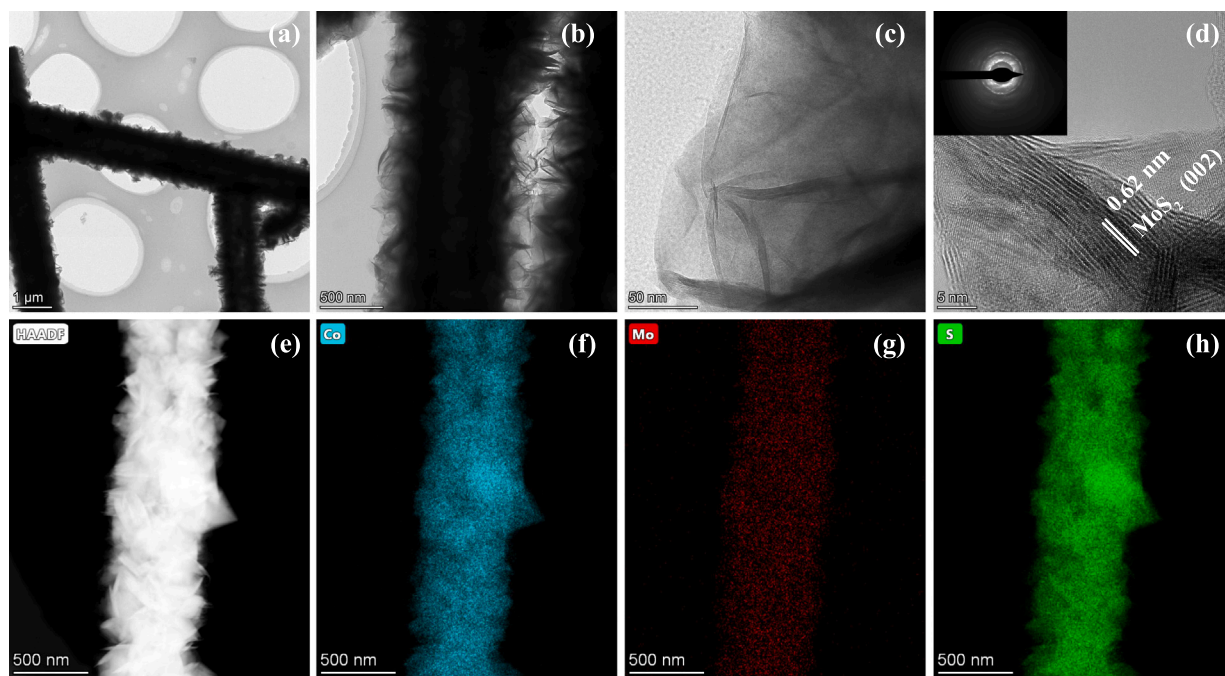


Fig. 4. (a)–(b) TEM and (c)–(d) HRTEM images of $\text{CoS}_2@\text{MoS}_2$ nanorods. STEM image of $\text{CoS}_2@\text{MoS}_2$ nanorod and the corresponding elemental mapping images of (e) HAADF, (f) Co, (g) Mo, (h) S, respectively.

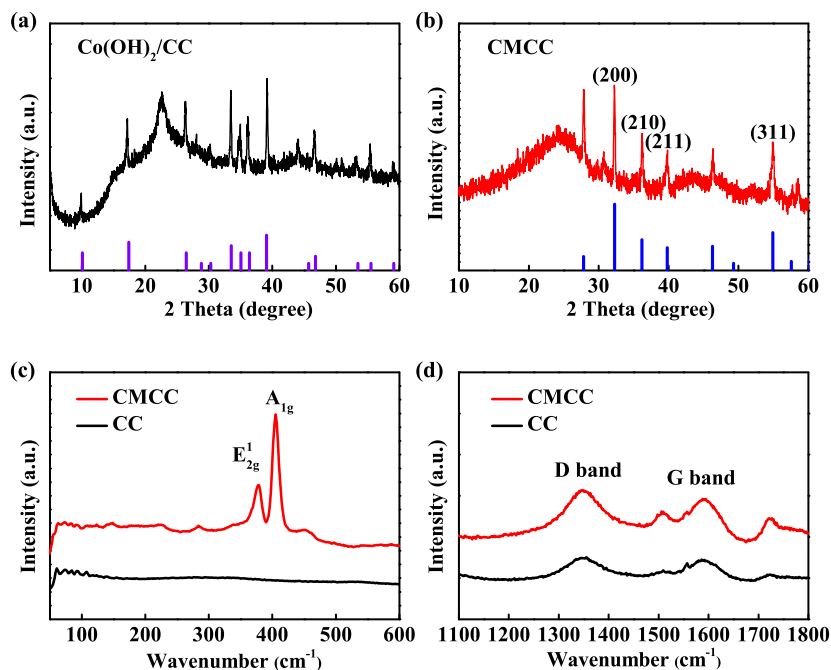


Fig. 5. (a)–(b) XRD patterns of the as-prepared $\text{Co(OH)}_2/\text{CC}$ and CMCC, respectively. (c)–(d) Raman spectra of the as-prepared CMCC and pure CC.

In order to further study the electrochemical performance of CMCC, it is used as a self-supporting electrode for lithium battery test. Therefore, the half cells are assembled in the glove box filled with argon, and lithium plate is used as counter electrode. Fig. 7a shows the rate performance of CMCC electrode and other samples at different constant currents. The specific capacity of $\text{CoS}_2@\text{MoS}_2$ loaded on the carbon cloth can be calculated by the formula: $C_{CM} = (C_T - C_{cc}) / M_{CM}$, where C_{CM} is the specific capacity of $\text{CoS}_2@\text{MoS}_2$, C_T is the total capacity of CMCC electrode, C_{cc} is the capacity of carbon cloth, and M_{CM} is the mass of $\text{CoS}_2@\text{MoS}_2$. The value of M_{CM} is obtained by the mass difference of CC before and after the reaction. Actually, the

cycle performance of bare carbon cloth proves that its contribution to capacity is tiny and can be ignored. Therefore, the lithium storage capacity is mainly provided by the loaded $\text{CoS}_2@\text{MoS}_2$, and M_{CM} is used as the calculation parameter.

The discharge specific capacity of the CMCC electrode is 1175, 1051, 903, 776, 655 and 386 mA h g^{-1} , corresponding to the test current density of 0.1, 0.2, 0.5, 1, 2 and 5 A g^{-1} , respectively. It should be noted that when the current density returns to 0.1 A g^{-1} , the specific capacity of CMCC electrode increases back to 1182 mA h g^{-1} , it shows good reversible performance. In contrast, the corresponding specific capacity of MoS_2/CC electrode at the current density of 0.1 to

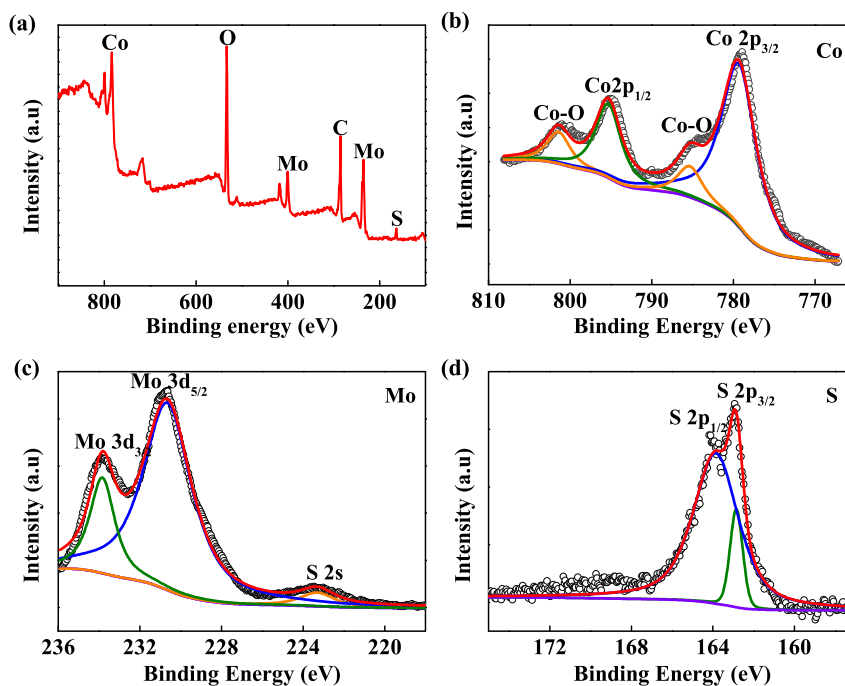


Fig. 6. (a) XPS spectrum of CMCC and high resolution scans of (b) Co 3d, (c) Mo 2p, (d) S 2p, respectively.

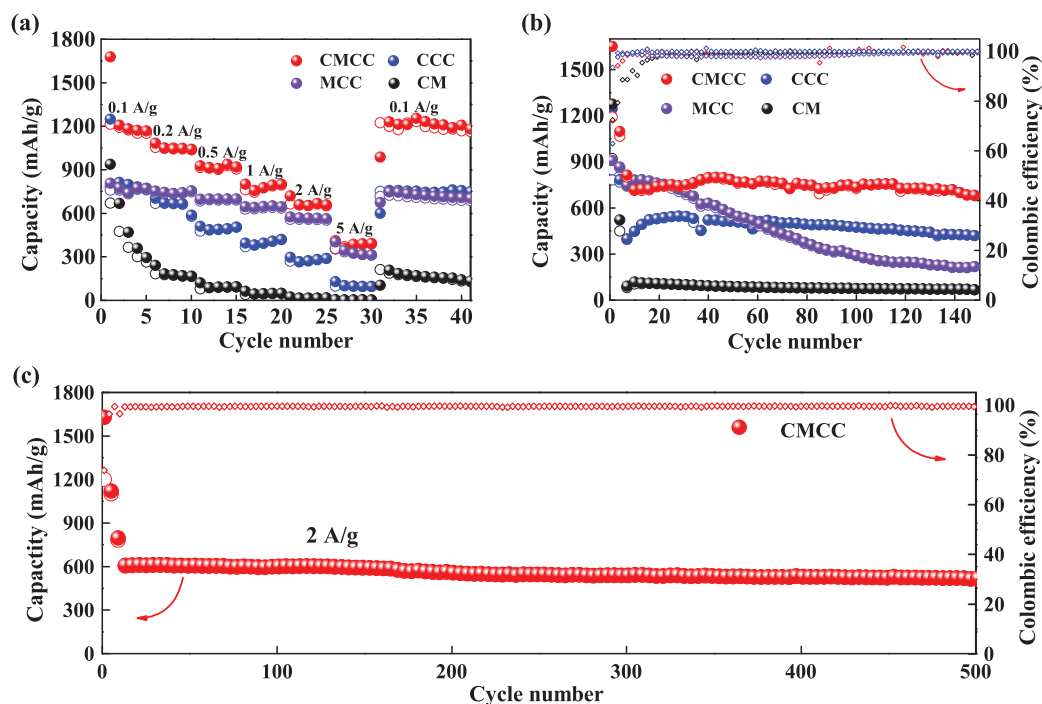


Fig. 7. (a) Rate performance of the four composite electrodes at different current densities. Cycling performance and coulombic efficiency of the as-prepared electrodes cycled at (b) 1 A/g for 150 cycles and (c) 2 A/g for 500 cycles, at 0.1 A/g for the first five cycles.

5 A g^{-1} is only 777, 738, 700, 648, 570, 317 mA h g^{-1} , respectively. The first cycle discharge capacity of CMCC is 1680 mA h g^{-1} at 0.1 A g^{-1} , which is also significantly higher than those from MoS_2/CC (MCC) and CoS_2/CC (CCC) based electrodes, and does not decay as rapidly as $\text{CoS}_2/\text{MoS}_2$ (CM). The cycling performance of CMCC, MCC, CCC and CM electrode at 0.1 A g^{-1} are shown in Fig. 7b. The first-turn discharge specific capacity and charge specific capacity of the CCC electrode are 1245 mA h g^{-1} and 783 mA h g^{-1} , respectively, and its coulombic efficiency is 63%. In contrast, the discharge/charge specific

capacity of the first cycle of CMCC is 1652 mA h g^{-1} and 1192 mA h g^{-1} , respectively, and the coulombic efficiency is about 72.1%. The above results indicate that the CMCC electrode has a more excellent reversible rate performance due to its unique structural characteristics. Specifically, the discharge capacity of CMCC remained at 706 mA h g^{-1} after 150 cycles, showing excellent cycle performance. However, the discharge specific capacity of MCC stabilized at about 780 mA h g^{-1} before the 20th cycle, then dropped sharply and finally remained at about 220 mA h g^{-1} . This result shows the poor performance of MCC

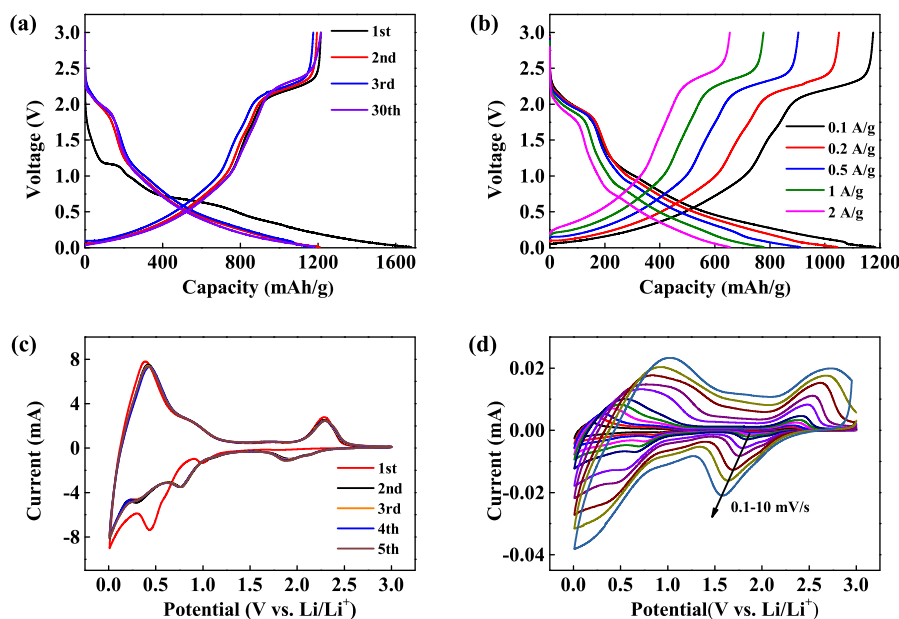


Fig. 8. The GDC profiles of CMCC electrode (a) for the 1st, 2nd, 3rd and 30th cycles at 0.1 A/g and (b) at the increasing discharge current density from 0.1 to 2.0 A/g. The CV curves of CMCC electrode (c) at a scan rate of 0.5 mV/s and (d) at different rates from 0.1 to 10 mV/s in the range of 0.01–3.0 V vs. Li/Li⁺.

during the electrochemical reaction and also proves that the CMCC electrode has a more stable structure. The long cycle performance of CMCC electrode is further tested at the current density of 2 A g⁻¹ (Fig. 7c). At this time, the initial discharge specific capacity of CMCC is 1680 mA h g⁻¹, and it can still reach about 600 mA h g⁻¹ after 500 cycles, showing strong cycle stability. The impressive cycle and rate performance of CMCC can be attributed to the unique topography and structure which enhances its ion transport dynamics. The coverage of uniform MoS₂ on the surface of CoS₂ NAs shortens the moving path of lithium ion and electron, and enhances the transfer of internal charge. In addition, the coating of large area MoS₂ nanoflakes can effectively prevent the agglomeration of the electrode during the reaction. The synergistic effect between MoS₂ nanosheets and CoS₂ nanorods can improve the stability of the electrode as well as the capacity.

The galvanostatic discharge/charge (GDC) process of CMCC electrode in the voltage range of 0.01–3.0 V at a current density of 0.1 A g⁻¹ is shown in Fig. 8a. Two obvious voltage plateau at ~1.13 V and ~0.5 V can be observed in the discharge reaction of first cycle. The discharge plateau at ~2.3 V and the charging plateau at ~1.95 V are observed in the following cycles. They are consistent with the cycling voltammetry (CV) curves, indicating the conversion between S and Li₂S. The irreversible capacity decrease in the first cycle may be due to the formation of solid electrolyte interphase (SEI) film. After that, the GDC curves of CMCC electrode are basically consistent until the 30th cycle, which manifests the prominent cycling ability of CMCC electrode. Fig. 8b shows the GDC curves at different current densities (0.1 A g⁻¹–2 A g⁻¹). Compared with Fig. 8a, the voltage plateau of these curves at different current densities has no hysteresis change. The similar plateau voltage indicates the stability of the reaction process. It can be found that with increasing the current density, the specific capacity decreases with the polarization of electrode materials, but the discharge specific capacity can still reach about 650 mA g⁻¹ at the current density of 2 A g⁻¹. It proves that CMCC electrode can support good lithium storage performance.

The first five cycles of CV curves at a scan speed of 0.5 mV/s show the lithium storage process of CMCC electrode (Fig. 8c). In the first cycle, there are three obvious peaks at ~1.77 V, ~0.98 V and ~0.44 V. The first two peaks indicate that Li⁺ is inserted into the outer layer of MoS₂ to form Li_xMoS₂ (MoS₂ + xLi⁺ + xe⁻ → Li_xMoS₂) [48], which is accompanied by the formation of irreversible SEI film [49]. The

latter represents the generation of Li₂S and metal Mo by the conversion reaction of Li_xMoS₂ (Li_xMoS₂ + (4-x)Li⁺ + (4-x)e⁻ → Li₂S + Mo). During the course of anodic reaction, an obvious peak at ~2.29 V can be observed, implying that Li₂S is oxidized to Li⁺ and sulfur. A new reduction peak at 1.9 V is observed in the following curves, indicating that S is reduced to Li₂S. The reduction peak of S shifts slightly in different cycles, which may be due to the activation of the material. The reaction process is consistent with the previous reports on the lithium storage mechanism of MoS₂, which clarifies the reaction mechanism. The subsequent CV curves basically coincide with each other, showing that the CMCC electrode has excellent cycling ability.

In order to further analyze the capacity performance of CMCC electrode, the kinetics mechanism is analyzed by studying the pseudocapacitance behavior. After testing at different rates (0.1–10 mV/s), the CV curves show the similar patterns in Fig. 8d. The capacitance effect can be analyzed by substituting current (*i*) and scanning rate (*v*) data to the following power exponential function formula: $i = av^b$ [50–52]. The value of *b* can be obtained by calculating the slope of log(*i*) and log(*v*) curves. When the value of *b* is close to 0.5, it indicates that the lithium storage process is dominated by diffusion behavior. When it is close to 1.0, the reaction mainly controlled changes into surface capacitance effect. For CMCC, Fig. 9a shows its log(*i*)-log(*v*) curves of redox reaction. It can be seen that the *b* values corresponding to the two most obvious peaks in the anodic and cathodic reactions are 0.89 and 0.96 respectively, which means that the electrochemical kinetics of CMCC electrode are mainly contributed by capacitive behavior [53]. To further quantitatively discuss the capacitance behavior during the reaction, the Dunn equation can be used to optimize the diffusion control part and the capacitance control part of the reaction. The equation is as follows: $i = k_1v^{1/2} + k_2v$ [54,55]. Note that the proportion of capacitance behavior (red area) after the fitting is indicated in the total current area (blue area) (Fig. S2†). The result shows that the capacitance contribution is 57.1% at the scanning speed of 0.1 mV/s. It is shown in Fig. 9b that when the scanning rate increases to 0.2, 0.3, 0.5, 0.7 and 1 mV/s, the capacitance behavior ratios are 61.2, 64.2, 70.5, 75.4 and 79.9%, respectively. It shows that the structure of CMCC provides good pseudocapacitance effect for the reaction system, which can realize the rapid transport of lithium ions.

To further understand its charge/discharge characteristics, the electrochemical impedance spectra (EIS) analysis of CMCC electrode is

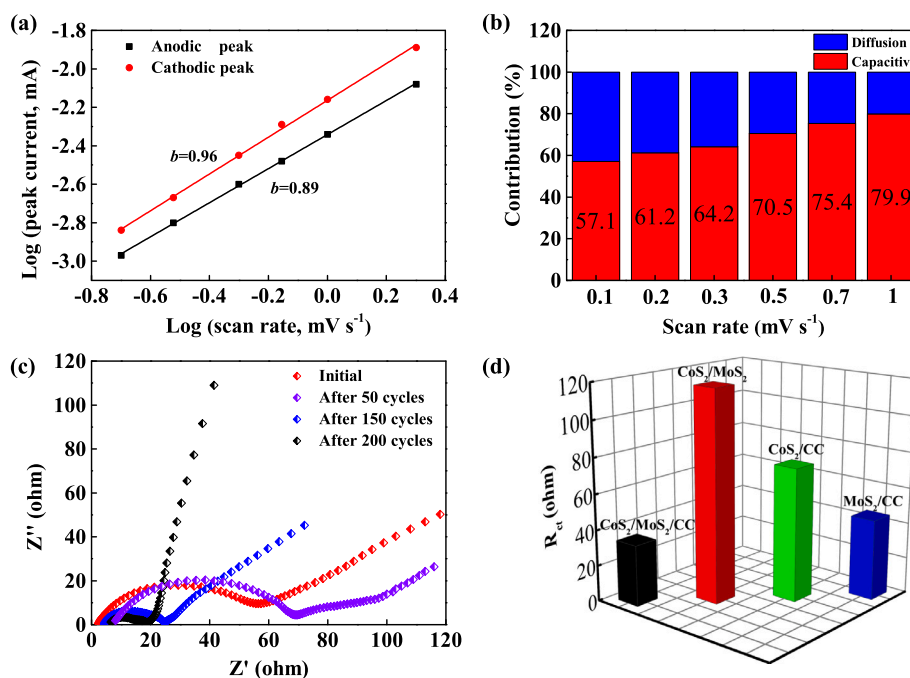


Fig. 9. (a) Graph of the logarithmic peak current and the logarithmic scan rate of the CMCC electrode. (b) The contribution of capacitance and diffusion control process at different scan rates of 0.1–1 mV/s. (c) Electrochemical impedance spectroscopy of CMCC electrode at different cycles. (d) Schematic diagram of the R_{ct} value of CoS₂@MoS₂/CC, CoS₂@MoS₂, CoS₂/CC and MoS₂/CC, respectively.

plotted in Fig. 9c. The Nyquist curve contains the semicircular part of the high/medium frequency region and the slope part of the low frequency region [56]. The former is caused by the SEI film resistance (R_f) and the charge transfer resistance (R_{ct}) at the electrode/electrolyte interface. The latter low frequency sloping line can be attributed to the Warburg impedance (W), which is related to the diffusion of lithium ions. Fig. S3† comprehensively lists the EIS spectra of different samples. It can be seen that the CMCC electrode has the smallest radius semicircle and steep inclined line, which describes the minimum charge transfer resistance and the ability to rapidly diffuse lithium ions. The detailed impedance parameters can be obtained by fitting the impedance spectrum with an analog circuit (Fig. S4†). Fig. 9d shows the fitting results of R_{ct} for different electrodes after the calculation. The R_{ct} of CMCC, CM, MCC and CCC electrodes are 34.2, 118, 45 and 74.7 Ω , respectively. The R_{ct} of CMCC is much smaller than that of the other three electrodes, which indicates that the structure of CMCC electrode has good electron transport capacity, and the results are consistent with the rate performance. Fig. 9c shows the impedance spectra of the CMCC electrode at different charging/discharging stages at the current density of 1 A g⁻¹. The Nyquist plot shows that the low frequency semi-circle becomes smaller as the number of cycles increases, which means a reduced charge transfer resistance. After 50 cycles, the value of R_{ct} remains basically unchanged. After 150 cycles, the value of R_{ct} decreases to 24.5 Ω , which may be caused by the activation of the electrode material. In addition, the Warburg impedance at 200 cycles is closer to 90°, indicating the excellent conductivity and enhanced dynamics of the CMCC electrode. In addition, the resistance in the low frequency region is linearly related to $\omega^{-1/2}$, and the corresponding relationship is:

$$Z' = K + \sigma\omega^{-1/2} \quad (3)$$

where K is a constant, ω is the frequency, and σ is the Warburg coefficient, which can be obtained from the slope of the curve in Fig. S3†. Furthermore, the lithium ion diffusion coefficient of each sample can be calculated by the following formula:

$$D = \frac{R^2 T^2}{2A^2 n^4 F^4 C^2 \sigma^2} \quad (4)$$

where D represents the diffusion coefficient, R , T , A , n , F and C represent the gas constant, the absolute temperature of the test environment, the area of the electrode material immersed in the electrolyte, the number of electrochemical reaction electrons, the Faraday constant and the concentration of lithium ions, respectively. The CMCC electrode in Fig. S5† has the smallest linear slope. Therefore, the fitting calculation shows that the lithium ion diffusion coefficient (0.82×10^{-12} cm² s⁻¹) of CMCC is significantly better than CCC (0.19×10^{-14} cm² s⁻¹), MCC (0.12×10^{-13} cm² s⁻¹) and CM electrode (0.54×10^{-15} cm² s⁻¹). It is further demonstrated that the electrode has good electronic transmission ability and conductivity under the coordination of the unique core-shell structure of CMCC. To further investigate the structural stability of CMCC, the electrode was analyzed by SEM and TEM tests. Fig. S6† shows the morphology of the sample at a current density of 2A/g after 200 cycles. As shown in Fig. S6†a and Fig. S6†b, CoS₂@MoS₂ still maintains a good nanorod structure and is densely distributed on the surface of CC, indicating that the CMCC electrode has robust cycling performance and structural stability. In addition, TEM tests illustrated that MoS₂ formed a shell layer on the surface of CoS₂ nanorods (Fig. 6c–d). Well-preserved core-shell structure can effectively reduce the volume expansion during the reaction and prevent the separation of active materials. This reveals that the structure of the CMCC electrode retains good structural integrity after 200 cycles, and this result also corresponds to the impedance curves.

The layered carbon cloth, as a substrate treated by oxygen plasma, has excellent conductivity and flexibility. It is an ideal carrier for loading and effectively alleviating the volume change of active materials. In the first step, the Co(OH)₂ nanowire arrays formed by hydrothermal method provide active sites for the subsequent reactions and contribute to further increasing the contact area between electrolyte and electrolyte. Finally, a uniform MoS₂ coating was formed on the surface of CoS₂ nanorods. There are many holes between these MoS₂ nanoflakes, which provide a larger reaction area for lithium storage reaction and form an interconnected electrochemical reaction network. At the same time, the protection layer can alleviate the agglomeration problem of MoS₂ to a certain extent. On the other hand, the incorporation of Co ions enhances the electrochemical conductivity and capacity of the

materials. The structure design shortens the ion transport distance in the reaction process and solves the problem of volume expansion on the basis of improving the capacity through synergetic effect, thus obtaining excellent cycle and rate performance.

4. Conclusion

In conclusion, a simple two-step hydrothermal method is designed to synthesize MoS₂ nanosheets on the surface of CoS₂ nanorods and grow on the surface of carbon cloth. The unique porous core-shell structure endows it with excellent negative potential of lithium battery, improving the conductivity and ensuring the stability of the structure. As shown by experimental characterization and pseudo capacitance calculation, the fabricated CMCC electrode exhibits remarkable cycle specific capacity and rate performance, and the coulomb efficiency of the first cycle is 70%. This design structure can be applied to the research of MoS₂ based materials and other TMSs materials, so as to promote its application and development in lithium batteries and other energy sources.

Declaration of competing interest

The authors declare that they have no known competing financial interests or personal relationships that could have appeared to influence the work reported in this paper.

Acknowledgments

This work was financially supported by the National Key R&D Program of China (Grants No. 2018YFB0406500, 2017YFA0303403, and 2019YFB2203400), the Natural Science Foundation of China (Grants Nos. 91833303, 61974043, 61805081, and 61674057), Projects of Science and Technology Commission of Shanghai Municipality, China (Grant Nos. 18JC1412400, 18YF1407200, 18YF1407000, and 19511120100), and the Program for Professor of Special Appointment (Eastern Scholar) at Shanghai Institutions of Higher Learning, China.

Appendix A. Supplementary data

Supplementary material related to this article can be found online at <https://doi.org/10.1016/j.cej.2020.127714>.

References

- [1] Y. Han, G.Y. Huang, Shengming Xu, Structural reorganization-based nanomaterials as anodes for lithium-ion batteries: Design, preparation, and performance, *Small* 16 (2020) 190284, <http://dx.doi.org/10.1002/sml.201902841>.
- [2] B. Scrosati, J. Hassoun, Y.K. Sun, A look into the future, *Energy Environ. Sci.* 4 (2011) 3287–3295, <http://dx.doi.org/10.1039/c1ee01388b>.
- [3] G.L. Zhu, C.Z. Zhao, J.Q. Huang, C.X. He, J. Zhang, S.H. Chen, L. Xu, H. Yuan, Q. Zhang, Fast charging lithium batteries: Recent progress and future prospects, *Small* 15 (2019) 1805389, <http://dx.doi.org/10.1002/sml.201805389>.
- [4] L.B. Hu, Y. Cui, Energy and environmental nanotechnology in conductive paper and textiles, *Energy Environ. Sci.* 5 (2012) 6423–6435, <http://dx.doi.org/10.1039/c2ee02414d>.
- [5] X.Y. Yu, L. Yu, X.W. Lou, Metal sulfide hollow nanostructures for electrochemical energy storage, *Adv. Energy Mater.* 6 (2016) 1501333, <http://dx.doi.org/10.1002/aenm.201501333>.
- [6] J.G. Wang, H.H. Sun, H.Y. Liu, D.D. Jin, X.R. Liu, X. Li, F.Y. Kang, Triaxial nanocables of conducting Polypyrrole@SnS₂@Carbon nanofiber enabling significantly enhanced Li-ion storage, *ACS Appl. Mater. Interfaces* 10 (2018) 13581–13587, <http://dx.doi.org/10.1021/acsmi.8b02111>.
- [7] K. Liang, K. Marcus, L. Guo, Z. Li, L. Zhou, Y. Li, S.T. De Oliveira, N. Orlovskay, Y.H. Sohn, Y. Yang, A freestanding NiS porous film as a binder-free electrode for Mg-ion batteries, *Chem. Commun.* 53 (2017) 7608–7611, <http://dx.doi.org/10.1039/c7cc03517a>.
- [8] Z. Chen, D.G. Yin, M. Zhang, Sandwich-like MoS₂@SnO₂@C with high capacity and stability for sodium/potassium ion batteries, *Small* 14 (2018) 170381, <http://dx.doi.org/10.1002/sml.201703818>.

- [9] J.P. Li, P. Wu, F.J. Lou, P. Zhang, Y.W. Tang, Y.M. Zhou, T.H. Lu, Mesoporous carbon anchored with SnS₂ nanosheets as an advanced anode for lithium-ion batteries, *Electrochim. Acta* 111 (2013) 862–868, <http://dx.doi.org/10.1016/j.electacta.2013.08.104>.
- [10] K.Y. Xie, K. Yuan, X. Li, W. Lu, C. Shen, C.L. Liang, R. Vajtai, P. Ajayan, B.Q. Wei, Superior potassium ion storage via vertical MoS₂ “Nano-Rose” with expanded interlayers on graphene, *Small* 13 (2017) 1701471, <http://dx.doi.org/10.1002/sml.201701471>.
- [11] H.L. Zhu, F. Zhang, J.R. Li, Y.B. Tang, Penne-like MoS₂/Carbon nanocomposite as anode for sodium-ion-based dual-ion battery, *Small* 14 (2018) 1703951, <http://dx.doi.org/10.1002/sml.201703951>.
- [12] X.H. Cao, C.L. Tan, X. Zhang, W. Zhao, H. Zhang, Solution-processed two-dimensional metal dichalcogenide-based nanomaterials for energy storage and conversion, *Adv. Mater.* 28 (2016) 6167–6196, <http://dx.doi.org/10.1002/adma.201504833>.
- [13] B.M. Sánchez, Y. Gogotsi, Synthesis of two-dimensional materials for capacitive energy storage, *Adv. Mater.* 28 (2016) 6104–6135, <http://dx.doi.org/10.1002/adma.201506133>.
- [14] K. Ma, H. Jiang, Y.J. Hu, C.Z. Li, 2D nanospace confined synthesis of pseudocapacitance-dominated MoS₂-in-Ti₃C₂ superstructure for ultrafast and stable Li/Na-ion batteries, *Adv. Funct. Mater.* 28 (2018) 1804306, <http://dx.doi.org/10.1002/adfm.201804306>.
- [15] H. Hwang, H. Kim, J. Cho, MoS₂ nanoplates consisting of disordered graphene-like layers for high rate lithium battery anode materials, *Nano Lett.* 11 (2011) 4826–4830, <http://dx.doi.org/10.1021/nl202675f>.
- [16] A.B. Laursen, S. Kegæs, S. Dahl, I. Chorkendorff, Molybdenum sulfides-efficient and viable materials for electro- and photoelectrocatalytic hydrogen evolution, *Energy Environ. Sci.* 5 (2012) 5577–5591, <http://dx.doi.org/10.1039/c2ee02618j>.
- [17] Y. Yan, X.M. Ge, Z.L. Liu, J.Y. Wang, J.M. Lee, X. Wang, Facile synthesis of low crystalline MoS₂ nanosheet-coated CNTs for enhanced hydrogen evolution reaction†, *Nanoscale* 5 (2013) 7768–7771, <http://dx.doi.org/10.1039/c3nr02994h>.
- [18] Y.G. Li, H.L. Wang, L.M. Xie, Y.Y. Liang, G.S. Hong, H.J. Dai, MoS₂ nanoparticles grown on graphene: An advanced catalyst for the hydrogen evolution reaction, *J. Am. Chem. Soc.* 133 (2011) 7296–7299, <http://dx.doi.org/10.1021/ja201269b>.
- [19] B. Luo, Y.X. Hu, X.B. Zhu, T.F. Qiu, L.J. Zhi, M. Xiao, H.J. Zhang, M.C. Zou, A.Y. Cao, L.Z. Wang, Controllable growth of SnS₂ nanostructures on nanocarbon surfaces for lithium-ion and sodium-ion storage with high rate capability†, *J. Mater. Chem. A* 6 (2018) 1462–1472, <http://dx.doi.org/10.1039/c7ta09757c>.
- [20] L.H. Li, Z.X. Deng, L.L. Yu, Z.Y. Lin, W.L. Wang, G.W. Yang, Amorphous transitional metal borides as substitutes for Pt cocatalysts for photocatalytic water splitting, *Nano Energy* 27 (2016) 103–113, <http://dx.doi.org/10.1016/j.nanoen.2016.06.054>.
- [21] J.G. Wang, R. Zhou, D.D. Jin, K.Y. Xie, B.Q. Wei, Uniform growth of MoS₂ nanosheets on carbon nanofibers with enhanced electrochemical utilization for Li-ion batteries, *Electrochim. Acta* 231 (2017) 396–402, <http://dx.doi.org/10.1016/j.electacta.2017.01.108>.
- [22] F. Zhou, S. Xin, H.W. Liang, L.T. Song, S.H. Yu, Carbon nanofibers decorated with molybdenum disulfide nanosheets: Synergistic lithium storage and enhanced electrochemical performance, *Angew. Chem. Int. Ed.* 53 (2014) 11552–11556, <http://dx.doi.org/10.1002/anie.201407103>.
- [23] C.B. Zhu, X.K. Mu, P.A.v. Aken, Y. Yu, J. Maier, Single-layered ultrasmall nanoplates of MoS₂ embedded in carbon nanofibers with excellent electrochemical performance for lithium and sodium storage, *Angew. Chem. Int. Ed.* 53 (2014) 2152–2156, <http://dx.doi.org/10.1002/anie.201308354>.
- [24] Y. Fang, Y.Y. Lv, F. Gong, A.A. Elzatahry, G.F. Zheng, D.Y. Zhao, Synthesis of 2D-Mesoporous-Carbon/MoS₂ heterostructures with well-defined interfaces for high-performance lithium-ion batteries, *Adv. Mater.* 28 (2016) 9385–9390, <http://dx.doi.org/10.1002/adma.201602210>.
- [25] X. Xu, Z.Y. Fan, X.Y. Yu, S.J. Ding, D.M. Yu, X.W. Lou, A nanosheets-on-channel architecture constructed from MoS₂ and CMK-3 for high-capacity and long-cycle-life lithium storage, *Adv. Energy Mater.* 4 (2014) 1400902, <http://dx.doi.org/10.1002/aenm.201400902>.
- [26] T. Xiong, H. Su, F. Yang, Q. Tan, P.B.S. Appadurai, A.A. Afuwape, K. Guo, Y. Huang, Z. Wang, M.-S. (Jie Tang) Balogun, Harmonizing self-supportive VN/MoS₂ pseudocapacitance core-shell electrodes for boosting the areal capacity of lithium storage, *Mater. Today Energy* 17 (2020) 100461, <http://dx.doi.org/10.1016/j.mtener.2020.100461>.
- [27] J.H. Feng, H. Zhou, J.P. Wang, T. Bian, J.X. Shao, A.H. Yuan, MoS₂ supported on MOF-derived carbon with core-shell structure as efficient electrocatalysts for hydrogen evolution reaction, *Int. J. Hydrogen Energy* 43 (2018) 20538–20545, <http://dx.doi.org/10.1016/j.ijhydene.2018.09.057>.
- [28] J.H. Feng, H. Zhou, D.Y. Chen, T. Bian, A.H. Yuan, Core-shell structured ZnCo/Ni@MoS₂ electrocatalysts for tunable hydrogen evolution reaction, *Electrochim. Acta* 331 (2020) 135445, <http://dx.doi.org/10.1016/j.electacta.2019.135445>.
- [29] Y.C. Huang, H. Yang, T.Z. Xiong, D. Adekoya, W.T. Qiu, Z.M. Wang, S.Q. Zhang, M.-Sadeeq Balogun (Jie Tang), Adsorption energy engineering of nickel oxide hybrid nanosheets for high areal capacity flexible lithium-ion batteries, *Energy Storage Mater.* 25 (2020) 41–51, <http://dx.doi.org/10.1016/j.ensm.2019.11.001>.

- [30] Y.C. Huang, Z.J. Guo, H. Liu, S.Q. Zhang, P.S. Wang, J. Lu, Y.X. Tong, Heterojunction architecture of N-doped WO_3 nanobundles with Ce_2S_3 nanodots hybridized on a carbon textile enables a highly efficient flexible photocatalyst, *Adv. Funct. Mater.* 29 (2019) 1903490, <http://dx.doi.org/10.1002/adfm.201903490>.
- [31] H.Y. Wang, D.Y. Ren, Z.J. Zhu, P. Saha, H. Jiang, C.Z. Li, Few-layer MoS_2 nanosheets incorporated into hierarchical porous carbon for lithium-ion batteries, *Chem. Eng. J. Interfaces* 288 (2016) 179–184, <http://dx.doi.org/10.1016/j.cej.2015.11.105>.
- [32] J.W. Zhou, J. Qin, X. Zhang, C.S. Shi, E.Z. Liu, J.J. Li, N.Q. Zhao, C.N. He, 2D space-confined synthesis of few-layer MoS_2 anchored on carbon nanosheet for lithium-ion battery anode, *ACS Nano* 9 (2015) 3837–3848, <http://dx.doi.org/10.1021/nn506850e>.
- [33] M.J. Li, Q.L. Deng, J.Y. Wang, K. Jiang, Z.G. Hu, J.H. Chu, In situ carbon encapsulation of vertical MoS_2 arrays with SnO_2 for durable high rate lithium storage: dominant pseudocapacitive behavior†, *Nanoscale* 10 (2018) 741–751, <http://dx.doi.org/10.1039/c7nr07359c>.
- [34] J.C. Wang, L.Y. Zhang, K. Sun, J.J. He, Y.J. Zheng, C.H. Xu, Y.X. Zhang, Y. Chen, M. Li, Improving ionic/electronic conductivity of MoS_2 Li-ion anode via manganese doping and structural optimization, *Chem. Eng. J.* 372 (2019) 665–672, <http://dx.doi.org/10.1016/j.cej.2019.04.203>.
- [35] X.M. Li, Z.X. Feng, J.T. Zai, Z.F. Ma, X.F. Qian, Incorporation of Co into MoS_2 /graphene nanocomposites: One effective way to enhance the cycling stability of Li/Na storage, *ACS Appl. Mater. Interfaces* 373 (2018) 103–109, <http://dx.doi.org/10.1016/j.jpowsour.2017.10.094>.
- [36] J.M. Son, S. Oh, S.H. Bae, S. Nam, I.K. Oh, A pair of NiCo_2O_4 and V_2O_5 nanowires directly grown on carbon fabric for highly bendable lithium-ion batteries, *Adv. Energy Mater.* 8 (2019) 1900477, <http://dx.doi.org/10.1002/aenm.201900477>.
- [37] J.W. Park, H.M. Zheng, Y.W. Jun, A.P. Alivisatos, Hetero-epitaxial anion exchange yields single-crystalline hollow nanoparticles, *J. Am. Chem. Soc.* 131 (2009) 13943–13945, <http://dx.doi.org/10.1021/ja905732q>.
- [38] C.B. Zhu, X.K. Mu, P.A.V. Aken, J. Maier, Y. Yu, Fast Li storage in MoS_2 -graphene-carbon nanotube nanocomposites: Advantageous functional integration of 0D, 1D, and 2D nanostructures, *Adv. Energy Mater.* 5 (2015) 1401170, <http://dx.doi.org/10.1002/aenm.201401170>.
- [39] X.R. Sun, H.W. Zhang, L. Zhou, X.D. Huang, C.Z. Yu, Polypyrrole-coated zinc ferrite hollow spheres with improved cycling stability for lithium-ion batteries, *Small* 12 (2016) 3732–3737, <http://dx.doi.org/10.1002/sml.201601143>.
- [40] Y.G. Sun, F. Alimohammadi, D.T. Zhang, G.S. Guo, Enabling colloidal synthesis of edge-oriented MoS_2 with expanded interlayer spacing for enhanced HER catalysis, *Nano Lett.* 17 (2017) 1963–1969, <http://dx.doi.org/10.1021/acs.nanolett.6b05346>.
- [41] Y.H. Lee, X.Q. Zhang, W.J. Zhang, M.T. Chang, C.T. Lin, K.D. Chang, Y.C. Yu, J.T.W. Wang, C.S. Chang, L.J. Li, T.W. Lin, Synthesis of large-area MoS_2 atomic layers with chemical vapor deposition, *Adv. Mater.* 24 (2012) 2320–2325, <http://dx.doi.org/10.1002/adma.201104798>.
- [42] C. Wang, W. Wan, Y.H. Huang, J.T. Chen, H.H. Zhou, X.X. Zhang, Hierarchical MoS_2 nanosheet/active carbon fiber cloth as a binder-free and free-standing anode for lithium-ion batteries†, *Nanoscale* 6 (2014) 5351–5358, <http://dx.doi.org/10.1039/c4nr00303a>.
- [43] R. Bose, Z.Y. Jin, S. Shin, S. Kim, S.Y. Lee, Y.S. Min, Co-catalytic effects of CoS_2 on the activity of the MoS_2 catalyst for electrochemical hydrogen evolution, *Langmuir* 33 (2017) 5628–5635, <http://dx.doi.org/10.1021/acs.langmuir.7b00580>.
- [44] C.B. Ouyang, S. Feng, J. Huo, S.Y. Wang, Three-dimensional hierarchical $\text{MoS}_2/\text{CoS}_2$ heterostructure arrays for highly efficient electrocatalytic hydrogen evolution, 2, 2017, pp. 134–141, <http://dx.doi.org/10.1016/j.jee.2017.01.004>.
- [45] C.B. Ouyang, X. Wang, S.Y. Wang, Phosphorus-doped CoS_2 nanosheet arrays as ultra-efficient electrocatalysts for the hydrogen evolution reaction†, *Chem. Commun.* 51 (2015) 14160–14163, <http://dx.doi.org/10.1039/c5cc05541e>.
- [46] P.P. Wang, H.Y. Sun, Y.J. Ji, W.H. Li, X. Wang, Three-dimensional assembly of single-layered MoS_2 , *Adv. Mater.* 26 (2014) 964–969, <http://dx.doi.org/10.1002/adma.201304120>.
- [47] Y.M. Chen, X.Y. Yu, Z. Li, U. Paik, X.W. Lou, Hierarchical MoS_2 tubular structures internally wired by carbon nanotubes as a highly stable anode material for lithium-ion batteries, *Sci. Adv.* 2 (2016) e160002, <http://dx.doi.org/10.1126/sciadv.1600021>.
- [48] L. Zhang, D. Sun, J. Kang, J. Feng, H.A. Bechtel, L.W. Wang, E.J. Cairns, J.H. Guo, Electrochemical reaction mechanism of the MoS_2 electrode in a lithium-ion cell revealed by in situ and operando X-ray absorption spectroscopy, *Nano Lett.* 18 (2018) 1466–1475, <http://dx.doi.org/10.1021/acs.nanolett.7b05246>.
- [49] L.Y. Ao, C. Wu, Y.N. Xu, X. Wang, K. Jiang, L.Y. Shang, Y.W. Li, J.Z. Zhang, Z.G. Hu, J.H. Chu, A novel Sn particles coated composite of SnOx/ZnO and N-doped carbon nanofibers as high-capacity and cycle-stable anode for lithium-ion batteries, *J. Alloys Compd.* 819 (2020) 153036, <http://dx.doi.org/10.1016/j.jallcom.2019.153036>.
- [50] C. Wu, Y.N. Xu, L.Y. Ao, K. Jiang, L.Y. Shang, Y.W. Li, Z.G. Hu, J.H. Chu, Robust three-dimensional porous rGO aerogel anchored with ultra-fine $\alpha\text{-Fe}_2\text{O}_3$ nanoparticles exhibit dominated pseudocapacitance behavior for superior lithium storage, *J. Alloys Compd.* 816 (2020) 152627, <http://dx.doi.org/10.1016/j.jallcom.2019.152627>.
- [51] E. Lim, H. Shim, S. Fleischmann, V. Presser, Fast and stable lithium-ion storage kinetics of anatase titanium dioxide/carbon onion hybrid electrodes†, *J. Mater. Chem. A* 6 (2018) 9480–9488, <http://dx.doi.org/10.1039/c8ta02293c>.
- [52] Q. Huang, T. Wei, M. Zhang, L.Z. Dong, A.M. Zhang, S.L. Li, W.J. Liu, J. Liu, Y.Q. Lan, A highly stable polyoxometalate-based metal-organic framework with $\pi\text{-}\pi$ stacking for enhancing lithium ion battery performance†, *J. Mater. Chem. A* 5 (2017) 8477–8483, <http://dx.doi.org/10.1039/c7ta00900c>.
- [53] S.H. Gao, G.S. Shi, H.P. Fang, Impact of cation- π interactions on the cell voltage of carbon nanotube-based Li batteries†, *Nanoscale* 8 (2016) 1451–1455, <http://dx.doi.org/10.1039/c5nr06456b>.
- [54] L.Y. Ao, C. Wu, X. Wang, Y.N. Xu, K. Jiang, L.Y. Shang, Y.W. Li, J.Z. Zhang, Z.G. Hu, J.H. Chu, Superior and reversible lithium storage of SnO_2 /graphene composites by silicon doping and carbon sealing, *ACS Appl. Mater. Interfaces* 12 (2020) 20824–20837, <http://dx.doi.org/10.1021/acsami.0c00073>.
- [55] C.M. Chen, Y.C. Yang, S.S. Ding, Z.X. Wei, X. Tang, P.C. Li, T.H. Wang, G.Z. Cao, M. Zhang, S-doped carbon@ TiO_2 to store Li^+/Na^+ with high capacity and long life-time, *Energy Storage Mater.* 13 (2018) 215–222, <http://dx.doi.org/10.1016/j.ensm.2018.01.015>.
- [56] Z.W. Xu, T. Wang, L. Kong, K. Yao, H. Fu, K. Li, L.Y. Cao, J.F. Huang, Q.L. Zhang, MoO_2 @ MoS_2 nanoarchitectures for high-loading advanced lithium-ion battery anodes, *Part. Part. Syst. Charact.* 34 (2017) 1600223, <http://dx.doi.org/10.1002/ppsc.201600223>.